

Simulation of a Single Red Blood Cell Flowing Through a Microvessel Stenosis Using Dissipative Particle Dynamics

L. L. Xiao^{*}, S. Chen^{*,†}, C. S. Lin^{*} and Y. Liu[‡]

Abstract: The motion and deformation of a single red blood cell flowing through a microvessel stenosis was investigated employing dissipative particle dynamics (DPD) method. The numerical model considers plasma, cytoplasm, the RBC membrane and the microvessel walls, in which a three dimensional coarse-grained spring network model of RBC's membrane was used to simulate the deformation of the RBC. The suspending plasma was modelled as an incompressible Newtonian fluid and the vessel walls were regarded as rigid body. The body force exerted on the free DPD particles was used to drive the flow. A modified bounce-back boundary condition was enforced on the membrane to guarantee the impenetrability. Adhesion of the cell to the stenosis vessel surface was mediated by the interactions between receptors and ligands. Firstly, the motion of a single RBC in a microfluidic channel was simulated and the results were found in agreement with the experimental data cited by [1]. Then the mechanical behavior of the RBC in the microvessel stenosis was studied. The effects of the bending rigidity of membrane, the size of the stenosis and the driven body force on the deformation and motion of red blood cell were discussed.

Keywords: Dissipative particle dynamics, Red blood cell, Microvessel stenosis, Deformation and motion.

1 Introduction

Red blood cells(RBCs) are small liquid capsules enclosed by a biological membrane consisting of a lipid bilayer and an underlying protein cytoskeleton. The major function of RBCs is to deliver oxygen to tissue and take away carbon dioxide to

^{*} School of Aerospace Engineering and Applied mechanics, Tongji University, No. 100 Zhangwu Road, Shanghai 200092, China.

[†] Corresponding Author. Email: schen_tju@mail.tongji.edu.cn

[‡] Department of Mechanical Engineering, The Hong Kong Polytechnic University, Hung Hom, Kowloon, HongKong, China.

the lungs. During its 4-month life span, a RBC circulates a million times in human body, often squeezing through narrow capillaries which are $3\sim 4\ \mu\text{m}$ in diameter. The RBC demonstrates extraordinary ability to undergoes severe deformation and fluidity (see, e.g. [1]). Its deformability is mainly dependent on the membrane mechanical properties. Variations in mechanical properties, especially in stiffness and viscosity, often decrease RBC deformability, which might lead to compromised blood flow through the microvascular system, [2-4], and trigger pathophysiological effects such as anemia, [5], and sepsis [6]. A study on the deformation of the RBC can lead to a better understanding of disease progression mechanisms and provide valuable knowledge for the study of hemorheology.

A healthy human RBC has a biconcave shape with a diameter of $8\ \mu\text{m}$ and a thickness of $2\ \mu\text{m}$. As a consequence of RBC size and deformability, the nature of blood flow changes greatly with the vessel diameter. The blood exhibits homogeneous non-Newtonian nature in large vessels and the size effect of the RBCs can be neglected. However, in vessels with smaller diameters, such as arterioles and venules, the size of a red blood cell is not negligible compared with the diameter of the blood vessel, and it has to be treated as a discrete elastic object suspended in plasma. Therefore, the detailed quantitative understanding of blood flow in micro-circulation requires explicit modeling of RBCs.

Numerous efforts have been made to describe the red blood cell motion and deformation in capillary. Several RBC deformation models have been developed. Pozrikidis [7] described the membrane of a RBC as a highly deformable two-dimensional shell without thickness. Another representative model is the coarse grained spring-based membrane network model developed by Pivkin and Karniadakis [8] and Fedosov et al. [9]. An example of a 3D implementation of the spring network approach is the worm-like chain, in which the coarse grained spring network exhibiting elastic and viscous response is consistent with the spectrin cytoskeleton structure, and bending stiffness is introduced in terms of the network bending energy. In their study, constraints on the cell surface area and volume are also imposed to ensure the area incompressibility of the lipid bilayer and the volume incompressibility of the interior liquid.

On the other hand, numerical methods have sought to describe cell behavior and deformation in a variety of flows. Pozrikidis [10] employed the boundary element method to study the transient deformation of liquid capsules in shear flows. Shen and He [11] employed the immersed boundary method together with lattice Boltzmann method to simulate the separation of RBCs at micro-vascular bifurcations. Shi et al. [12] employed a lattice Boltzmann fictitious domain method to deal with multiple cells behavior in flow. Zhang and Zhang [13] used a moving mesh technology to simulate the behavior of the RBC in microvessel stenosis. Fedosov et al.

[14] used a dissipative particle dynamics with coarse-grained method to establish the RBC model to study the effects of cell deformability and adhesive dynamics of infected RBCs. Noguchi and Gompper [15] employed multiparticle collision dynamics to simulate the shape transitions of RBCs in capillary flows.

In light of the complexity of cell motion and deformation in microvessels, numerical simulations on the mechanical behavior of RBCs under flow in microvessels could serve as a valuable tool for quantifying the biomechanical parameters of RBCs. Vahidkhah and Fatourae [16] reported that increasing cell-cell adhesion strength together with geometrical effects of the stenosed channel leads to the formation of cell aggregates. Wang and Xing [17] explored the dependence of the transitions from slipper like to bullet like shapes at the stenosed zone of the vessel on the elastic properties of the erythrocyte membrane. In addition, due to increasing applications of micro-fluidic devices in medical diagnostics, [18], cellular deformation in confined environment has attracted much attention. Cells forced through micro-fluidic constriction offer the potential means of quantifying cell mechanical characteristics in vitro, [19]. Multiple parameters, such as transit time, elongation and recovery time, in association with cell deformability can be quantified. For instance, diseased cells such as cancer cells are known to have different stiffness and elasticity compared to their healthy counterparts, [20-21]. Such differences could be used to distinguish between normal and cancer cells.

In the present study, the behaviors of a 3D deformable RBC in a stenosed microvessel were simulated by DPD method together with the coarse-grained spring network RBC model proposed by Pivkin and Karniadakis [8] and Fedosov et al. [9]. The objective of this paper is to establish fundamental understanding of the mechanisms of a single RBC through the microvessel stenosis. The deformation of a single RBC in the microfluidic channel is firstly simulated and compared with the experimental data cited by Li et al. [1]. Then, the microvessel stenosis with a rigid tube with converging-expanding zone was constructed. The motion of the cell passing through the microvessel stenosis was investigated. The effects of the vessel size, the cell membrane properties and the body force on the behaviors of the RBC through the microvessel stenosis were also analyzed.

2 Red blood cell model

A series of experiments have shown that RBCs subject to a transient shear flow recover a biconcave shape after relaxing, in which the rim of the cell is always formed by the same part of the membrane. These results suggest that there is an elastic energy stored in the membrane components that has a minimum when the RBC is in discocyte state and that local components of the membrane are not strained in the biconcave resting shape, [22-24]. Therefore, a healthy unstressed RBC has a

biconcave equilibrium shape with the minimum energy and is described by

$$z = \pm D_0 \sqrt{1 - \frac{4(x^2 + y^2)}{D_0^2}} \left[a_0 + a_1 \frac{x^2 + y^2}{D_0^2} + a_2 \frac{(x^2 + y^2)^2}{D_0^4} \right] \quad (1)$$

Where $D_0 = 7.82\mu\text{m}$ is the average diameter, $a_0 = 0.0518$, $a_1 = 2.0026$, and $a_2 = -4.491$. The surface area and volume of the RBC are equal to $135\mu\text{m}^2$ and $94\mu\text{m}^3$, respectively. The membrane network structure is generated by triangulating the unstressed equilibrium shape described by Eqn. 1. The initial biconcave cell shape is first imported into the grid generation software GAMBIT to generate unstructured grid, so the membrane is discretized into a number of triangle elements formed by a series of nodes. The vertex coordinates of the triangle elements are regarded as the membrane particles initial positions. Fig. 1 shows the network model of RBC, the vertexes are connected by wormlike springs.

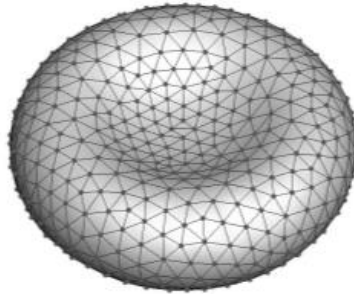


Figure 1: The network model of RBC.

The total energy of the network consists of an in-plane elastic energy, a bending energy, a surface area energy, and a volume energy, [1,8,9]:

$$E(\{\mathbf{r}_i\}) = E_{\text{in-plane}} + E_{\text{bending}} + E_{\text{area}} + E_{\text{volume}}, \quad (2)$$

Where $\{\mathbf{r}_i\}$ are a set of points with Cartesian coordinates, $i = 1 \dots N_v$, N_v is the number of the vertexes.

We employed the worm-like chain (WLC) model in combination with a power function potential. The in-plane elastic energy is given by

$$E_{\text{in-plane}} = \sum_{i=1, N_s} U_s(l_i) + \sum_{i \in 1, N_s} \frac{k_p}{(m-1) l_i^{m-1}} \quad (3)$$

Where N_s is the number of the springs; l_i is the length of the spring. The first term stands for the in-plane spring energy and the second term expresses a stored elastic

energy assigned to each triangular patch. k_p is a spring constant and m is a specified exponent, here we set it to 2.

The WLC energy is given by

$$U_{WLC} = \frac{k_B T l_{\max}}{4p} \frac{3x_1^2 - 2x_1^3}{1 - x_1}, \quad (4)$$

Where $x_1 = l/l_{\max} \in (0, 1)$, l_{\max} is the maximum spring extension, which is equal to 2.2 times equilibrium spring length for the WLC model, p is the persistence length, k_B is Boltzmann constant and T is temperature of the system, which is equal to 296K.

We derived the force corresponding to the in-plane energy at point o ,

$$\mathbf{F}_{o\text{-in-plane}} = \sum_{j \in 1, N_{o-s}} \left[-\frac{k_B T}{4p} \frac{4x_1^3 - 9x_1^2 + 6x_1}{(1 - x_1)^2} + \frac{k_p}{l_j^2} \right] \frac{\partial l_j}{\partial \mathbf{r}_o} \quad (5)$$

Where N_{o-s} is the number of the springs connected to point o , r_o is the position of point o .

The bending energy is concentrated at the element edges according to the bending potential

$$E_{\text{bending}} = \sum_{i \in 1, N_s} k_{\text{bend}} [1 - \cos(\theta_i - \theta_0)] \quad (6)$$

Where k_{bend} is a bending modulus; θ_i is the instantaneous angle formed between the outer normal vectors of two adjacent triangles α , β sharing the i th edge; θ_0 is the spontaneous angle. $\cos \theta_i = \mathbf{n}_\alpha \cdot \mathbf{n}_\beta$, $\sin \theta_i = \pm |\mathbf{n}_\alpha \times \mathbf{n}_\beta|$, which “+” is satisfied with $(\mathbf{n}_\alpha - \mathbf{n}_\beta) \cdot (\mathbf{r}_\alpha - \mathbf{r}_\beta) \geq 0$, where \mathbf{n}_α , \mathbf{n}_β are the outer normal vectors of triangle α and β , \mathbf{r}_α , \mathbf{r}_β are the centroid vectors of the two triangles, respectively.

The displacement of point o not only directly affects the bending energy of triangles connected to point o but also affects the bending energy of those outside triangles related to this displacement. Fig. 2 illustrates the deformation caused by the displacement at point o . Therefore, the force corresponding to the bending energy is expressed by

$$\mathbf{F}_{o\text{-bending}} = -\frac{\partial E_{\text{bending}}}{\partial \mathbf{r}_o} = -\sum_{i \in 1, N_o} k_{\text{bend}} (\sin \theta_k \cos \theta_0 - \cos \theta_k \sin \theta_0) \frac{\partial \theta_k}{\partial \mathbf{r}_o} \quad (7)$$

Where N_o is the number of triangles affected by the displacement of point o , θ_k is the angle between the unit normal vectors of the triangles.

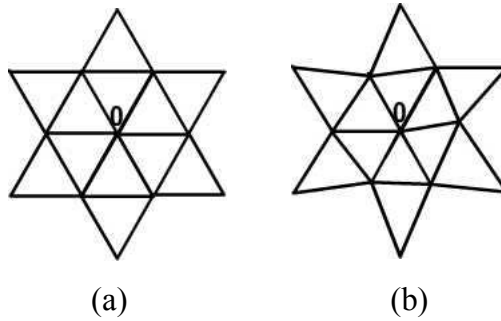


Figure 2: A contrast of the triangle network surrounding point o (a) before the displacement (b) after the displacement.

The last two terms in Eqn. 2 are used to constrain the variation of the surface area and the volume of the RBC. They are expressed as follows:

$$E_{\text{area}} = \frac{k_{\text{area}}^{\text{tot}}(A - A_0^{\text{tot}})^2}{2A_0^{\text{tot}}} + \sum_{j \in 1, N_t} \frac{k_{\text{area}}(A_j - A_0)^2}{2A_0}, \quad (8)$$

$$E_{\text{volume}} = \frac{k_{\text{volume}}(V - V_0^{\text{tot}})^2}{2V_0^{\text{tot}}}, \quad (9)$$

Where $k_{\text{area}}^{\text{tot}}$, k_{area} and k_{volume} are constraint constants for global area, local area, and volume; N_t is the number of the triangle elements; A and V are the instantaneous membrane area and cell volume; A_0^{tot} and V_0^{tot} are their specified total area and volume values, respectively. A_j , A_0 are the instantaneous and initial local area. The nodal forces corresponding to the surface area energy and volume energy are derived as follows:

$$\mathbf{F}_{\text{o-area}} = -\frac{\partial E_{\text{area}}}{\partial \mathbf{r}_o} = -\sum_{j \in 1, N_o} \left[\frac{k_{\text{area}}^{\text{tot}}(A - A_0^{\text{tot}})}{A_0^{\text{tot}}} + \frac{k_{\text{area}}(A_j - A_0)}{A_0} \right] \frac{\partial A_j}{\partial \mathbf{r}_o}, \quad (10)$$

$$\mathbf{F}_{\text{o-volume}} = -\frac{\partial E_{\text{volume}}}{\partial \mathbf{r}_o} = -\sum_{j \in 1, N_o} \frac{k_{\text{volume}}(V - V_0^{\text{tot}})}{V_0^{\text{tot}}} \frac{\partial V_j}{\partial \mathbf{r}_o} \quad (11)$$

Based on the analysis above, the force acting upon point o is expressed as follows:

$$\mathbf{F}_o = \mathbf{F}_{\text{o-inplane}} + \mathbf{F}_{\text{o-bending}} + \mathbf{F}_{\text{o-area}} + \mathbf{F}_{\text{o-volume}}, \quad (12)$$

For more details, please see references [8-9].

3 DPD governing equations

DPD is a mesoscopic particle-based simulation method. Details of the DPD formulation have been extensively described, [25-27]. Briefly, each particle represents a molecular cluster rather than an individual atom, and can be thought of as a soft lump of fluid. The DPD system consists of N point particles of mass m_i , position \mathbf{r}_i and velocity \mathbf{v}_i . DPD particles interact through three forces: conservative (\mathbf{F}_{ij}^C), dissipative (\mathbf{F}_{ij}^D), and random (\mathbf{F}_{ij}^R) forces given by the authors' names, should be centered in the document.

$$\begin{aligned}\mathbf{F}_{ij}^C &= F_{ij}^C(r_{ij})\hat{\mathbf{r}}_{ij}, \\ \mathbf{F}_{ij}^D &= -\gamma\omega^D(r_{ij})(\mathbf{v}_{ij} \cdot \hat{\mathbf{r}}_{ij})\hat{\mathbf{r}}_{ij}, \\ \mathbf{F}_{ij}^R &= -\sigma\omega^R(r_{ij}) \cdot \frac{\xi_{ij}}{\sqrt{dt}} \cdot \hat{\mathbf{r}}_{ij},\end{aligned}\tag{13}$$

where $\hat{\mathbf{r}}_{ij} = \mathbf{r}_{ij}/r_{ij}$, $\mathbf{r}_{ij} = \mathbf{r}_i - \mathbf{r}_j$ and $\mathbf{v}_{ij} = \mathbf{v}_i - \mathbf{v}_j$. The coefficients γ and σ define the strength of dissipative and random forces, respectively. In addition, ω^D and ω^R are weight functions, and ξ_{ij} is a normally distributed random variable with zero mean, unit variance, and $\xi_{ij} = \xi_{ji}$. All forces are truncated beyond the cutoff radius r_c , which defines the length scale in the DPD system. The conservative force is given by

$$F_{ij}^C(r_{ij}) = \begin{cases} a_{ij}(1 - r_{ij}/r_c) & \text{for } r_{ij} \leq r_c \\ 0 & \text{for } r_{ij} > r_c \end{cases}\tag{14}$$

where a_{ij} is the conservative force coefficient between particles i and j .

The random and dissipative forces form a thermostat and must satisfy the fluctuation-dissipation theorem in order for the DPD system to maintain equilibrium temperature T . This leads to:

$$\omega^D(r_{ij}) = [\omega^R(r_{ij})]^2, \quad \sigma^2 = 2\gamma k_B T\tag{15}$$

The choice for the weight functions is as follows

$$\omega^R(r_{ij}) = \begin{cases} (1 - r_{ij}/r_c)^k & \text{for } r_{ij} \leq r_c \\ 0 & \text{for } r_{ij} > r_c \end{cases}\tag{16}$$

where $k=1$ for the original DPD method. However, other choices (e.g., $k=0.25$) for these envelopes have been used, [28], in order to increase the viscosity of the DPD fluid.

The time evolution of velocities and positions of particles is determined by the Newton's second law of motion

$$d\mathbf{r}_i = \mathbf{v}_i dt\tag{17}$$

$$d\mathbf{v}_i = \sum_{j \neq i} (\mathbf{F}_{ij}^C + \mathbf{F}_{ij}^D + \mathbf{F}_{ij}^R) dt + \mathbf{F}_{\text{ext}} dt \quad (18)$$

Where \mathbf{F}_{ext} is the external force acting upon on the particle i .

The above equations of motion were integrated using the modified velocity-Verlet algorithm, [29].

4 Model and physical units scaling

The scaling procedure relates the model's non-dimensional units to physical units. In order to keep the simulation system consistent with the real system, the physical properties should be mapped onto the dimensionless properties in the model. The length scale is adapted, [8-9]:

$$L^S = \frac{D_0^P}{D_0^M}, \quad (19)$$

Where the superscript M and P denote "model" and "physical". The real RBC has an average diameter $D_0^P = 7.82 \mu m$ and we define the RBC with diameter $D_0^M = 7.82$ in the model.

The energy scale is provided as follows

$$E^S = \frac{Y^P}{Y^M} \left(\frac{D_0^P}{D_0^M} \right)^2, \quad (20)$$

where the Young's modulus Y is employed for the given area constraint parameters $k_{\text{area}}^{\text{tot}}$ and k_{area} , [30]. Y^P and Y^M are set to $18.9 \mu N/m$ and 392.453 respectively, [30].

The force scale is defined by

$$N^S = \frac{Y^P}{Y^M} \frac{D_0^P}{D_0^M}, \quad (21)$$

The scaling between model and physical times is defined as follows

$$\tau^S = \frac{Y^M}{Y^P} \frac{D_0^P}{D_0^M} \frac{\eta^P}{\eta^M}, \quad (22)$$

Where η^P is the physical fluid viscosity, the viscosities of plasma and cytoplasm are set to $1.2 \times 10^{-3} Pa \cdot s$ and $6 \times 10^{-3} Pa \cdot s$, respectively. Since $k = 0.25$ is employed in Eqn. 16 and according to reference literature, [31], the model fluid viscosity is defined by

$$\eta^M = \frac{315 k_B T}{128 \pi \gamma r_c^3} + \frac{512 \pi \gamma n^2 r_c^5}{51975}, \quad (23)$$

5 Boundary conditions

The cell membrane encloses a viscous fluid and is surrounded by the plasma. To prevent mixing between the internal and external fluids, membrane impenetrability is required. We perform reflections of the fluid particles at the triangular plaquettes that form the RBC membrane. Fig. 3 shows a moving particle p and a triangular element. In order to find out whether a specific particle will pass through a specified element or not, we use the dot product of the element normal vector and the vector connected the positions of the moving particle and one of the three vertexes of the triangular element. If the product of dot products at initial time and next time step is negative, the particle will be considered to cross the moving plane and then we enforce the bounce-back reflection. The reflections are performed every time step of temporal integration since in DPD each particle moves with constant velocity within a single time step.

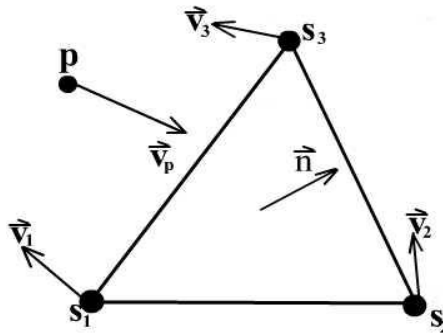


Figure 3: Sketch of a moving particle and a triangular element.

Another boundary condition, which should be focused on, is interaction between the cell membrane and the microvessel stenosis. When the RBC approaches the stenosis, it binds to the wall. However, when adhered RBC is exposed simultaneously to other forces stronger than the binding forces, the bonds break. Adhesion of the RBC to the vessel is mediated by the interactions between receptors and ligands which are the adhesion sites distributed on the surface of the cell and the microvessel stenosis respectively, [14]. Bonds between receptors and ligands may be formed if they are close enough to each other. As an approximation, we model the attractive force with a linear spring attached to the RBC's surface. During the simulation the receptor or ligand interactions are considered every time step. The formation and dissociation of bonds between receptors and ligands are determined according to the probability.

6 RBC in the microfluidic channel

In this section, two different sets of cases were considered. In the first one, a healthy human RBC through a microfluidic channel is simulated and compared with the experiment cited by Li et al. [1]. The experiment shows the shape evolution of an RBC as it is squeezed through a $4\mu\text{m} \times 4\mu\text{m}$ channel under a pressure difference of 1.5mm of water. The computational domain in the present study is demonstrated in Fig. 4.

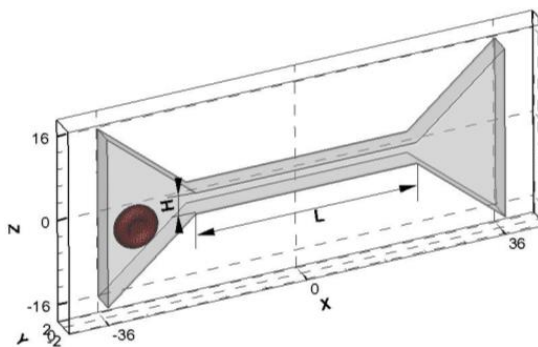


Figure 4: Geometry of the computational domain in a three-dimensional microfluidic channel.

The length and height of the narrowest part of the channel are $L=40\mu\text{m}$ and $H=4\mu\text{m}$. The length, width and height of the whole channel are $72\mu\text{m}$, $4\mu\text{m}$ and $32\mu\text{m}$. The membrane consists of 644 DPD particles and the number density of the cytoplasm is $n=10$. The RBC is suspended in a solvent which consists of free DPD particles with number density $n=4$. We enforce the periodic condition on the flow of x axis direction. Three layers of wall particles are arranged on the channel surface to implement the no-slip boundary condition. The channel wall is assumed to be rigid and the plasma is assumed to be homogeneous, incompressible, and Newtonian fluid. The dimensionless body force exerted on the particles in straight zone is 1.

The RBC experiences severe deformation when it squeezing through the channel. When the RBC enters the constriction, its leading end looks like being absorbed into the narrowest channel. In order to squeeze through the channel with the smaller size than the RBC's diameter, the RBC folds itself to fit the constriction and is elongated in the flow direction. When the RBC exits from the constriction, it recovers biconcave shape. According to the contrasts between the experiment and simulation, it is found that the conformations in different specified positions are nearly in agreement, as shown in Fig. 5.

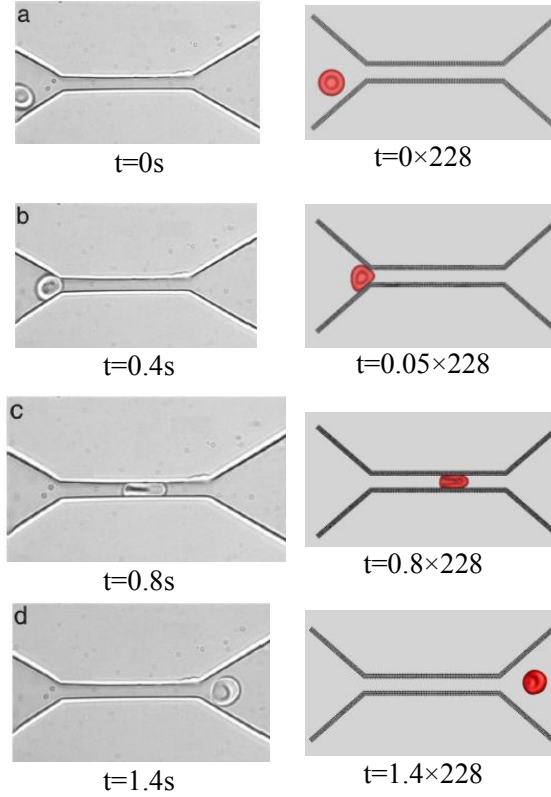


Figure 5: Deformation comparisons of RBC transiting through the microfluidic channel between experiment and DPD simulation.

There exists a difference between the experiment and simulation on the time when the RBC approaches the entrance of the constriction. It takes less time for RBC to transit from the initial position to the constriction in the simulation. Maybe it is relevant to the boundary condition enforced on the inlet and the experimental condition. It demonstrates that the RBC model can be used to simulate the large deformation in the confined environment.

7 RBC in the microvessel stenosis

RBC motion and deformation in microvessel stenosis are analyzed in this section. The computational domain is demonstrated in Fig. 6. A single cell is placed inside a tube with length of $L=50\mu\text{m}$ and diameter of $D=10\mu\text{m}$, necking down to a local diameter D_{min} . The length of the stenosis is $L_{neck} = 14.928\mu\text{m}$. The axial distance

between the front end of RBC and the entrance is represented by Y_d . The length of the RBC in the flow direction is illustrated by L_{max} . A dimensionless body force along the flow direction was exerted on each fluid DPD particle.

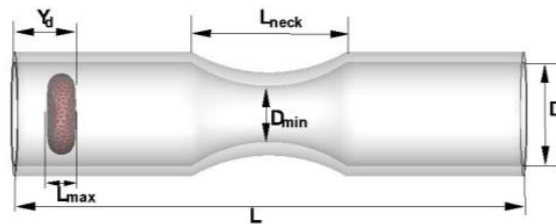


Figure 6: Geometry of the stenosed tube.

First, a single RBC is introduced at $Y_d = 6.25\mu m$ in a stenosed tube with $D_{min} = 6\mu m$ and 615 nodes are used to discretize the membrane. The cell deformation experiences several stages through the vessel stenosis. Figs. 7(a)~(b) show that the RBC shape transits from biconcave to parachute in the straight tube. The cell is significantly distorted as it moves through the narrow neck and the membrane is drawn out forming slipper-like corrugations, as shown in Fig. 7(c). A bullet-like shape develops when the cell approaches the neck region in Fig. 7(d). Figs. 7(d)~(e) show that the RBC rotates and becomes quite horizontal while passing through the stenosed zone. It exhibits the asymmetric behavior in the symmetric flow, which is consistent with [32]. It begins relaxing when the cell exits the neck region and a biconcave shape is recovered, as shown in Fig. 7(f). The time for the process of the cell entering the converging zone is greater than that for the cell exiting the expanding zone, as shown in Figs. 7(c)~(d) and Figs. 7(d)~(e). This is mainly dependent on the shape of the RBC. The structure of the converging part constrains RBC, so it flows slowly. The RBC has to change its shape to adapt the geometry of the channel. The middle part of the RBC is stretched by the plasma to fit the constriction of the channel and the energy stored in the membrane increased the resistance force for RBC. However, during the period of RBC exiting from the expanding zone, the constraint force by the tube stenosis become smaller with the diameter increased. The energy of the membrane drives RBC to transit through the stenosis.

In the next simulation, different values of the bending constant related to membrane bending rigidity were employed to investigate the effect of the membrane stiffness on the transit time of the RBC. Three dimensionless bending constants are used for the investigation: 57.544, 28.772 and 5.7544 which are corresponding to bending rigidity of $2.4 \times 10^{-18}J$, $1.2 \times 10^{-18}J$ and $2.4 \times 10^{-19}J$, respectively, [30]. Fig. 8

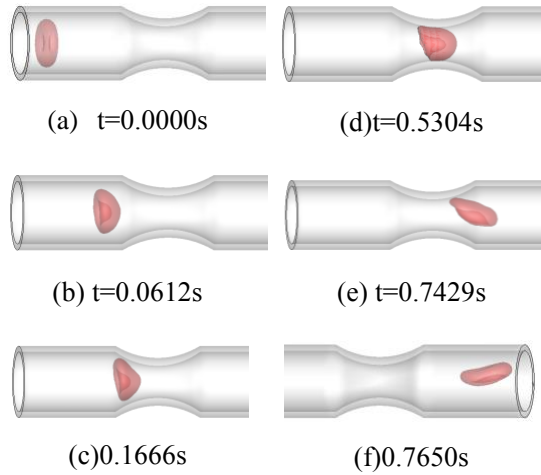


Figure 7: Variation of the RBC shape in the microvessel stenosis.

shows the position of the front end of RBC plotted as a function of time. There is nearly no difference on the time used to flow through straight tube for RBCs of different bending rigidities. The time from the front end of RBC entering the converging zone to the back end of RBC exiting from the expanding zone, for high rigidity RBC is about 0.70s and for low rigidity RBC is about 0.65s. It provides a quantitative understanding of the effect of bending rigidity on RBC transiting through the microvessel stenosis.

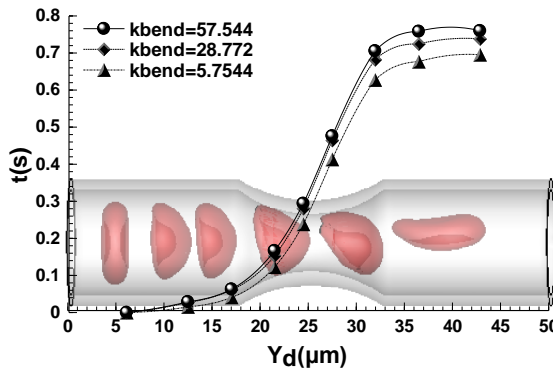


Figure 8: Variation of the position of the front end of RBC with the time at different bending constants.

At last, the effects of the driven force and the structural parameters of the stenosed tube on RBC deformation flowing in microvessel stenosis are investigated. The deformation of RBC in response to the external environmental factors is measured by L_{max} . Variation of RBC axial length with time at different values of driven force of 1, 2, 4 in the microvessel with the minimal diameter $D_{min} = 4\mu m$ is illustrated in Fig. 9. The distance of front end of the RBC from the inlet of the tube is $12\mu m$.

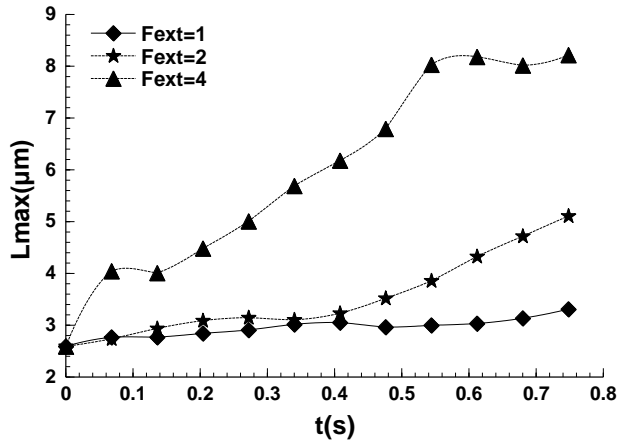


Figure 9: RBC axial length variation with the time at different values of driven force.

Fig. 9 shows that the higher the driven force, the greater the axial length of RBC at the same time. But the RBC deformation is not linearly correlated with the driven force. The slope of the curve represents the deformation rate of the RBC. The RBC deforms quickly at the higher driven force. The driven force represents the blood pressure difference. It takes less time for RBC to transit through the microvessel stenosis under the high blood pressure difference.

Fig. 10 shows that the RBC is placed at $Y_d = 12\mu m$ in the stenosed tubes with different sizes of D_{min} and the dimensionless driven force is set to 2. By comparison of the axial length in different tubes at the same time, it is found that the bigger the size of D_{min} , the smaller the axial length of RBC. It takes less time for RBC in large size of stenosis to approach the same position in different size of tubes. When the minimal diameter of the microvessel stenosis $D_{min} = 6\mu m$ is decreased to $D_{min} = 4\mu m$, the healthy RBC needs a longer time to stretch itself to fit the narrowed vessel unless the blood pressure becomes higher by comparing Fig. 9 with Fig. 10.

The analysis about the effects of different factors on the deformation of RBC will

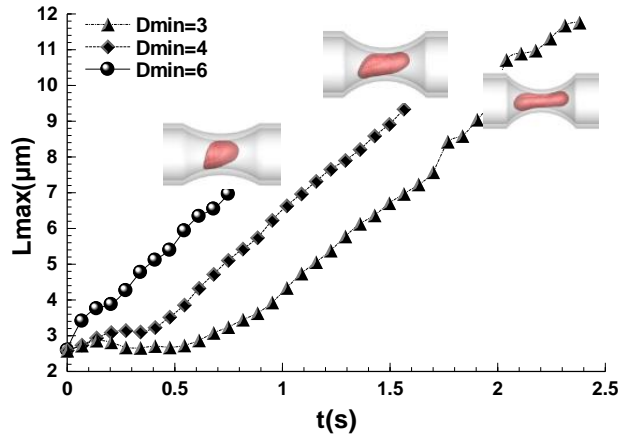


Figure 10: RBC axial length variation with the time at different sizes of D_{min} .

provide the foundation for the study of thrombosis from the mechanical point of view. The diseased RBC with high stiffness flows more slowly than the healthy RBC in the microvessel stenosis. Gradually, the accumulation of diseased RBCs forms in the microvessel stenosis and it would decelerate the microcirculation flow and consequently contribute to microvascular obstruction. In addition, it takes a longer time for the RBC deforming itself to transit through the tube stenosis with smaller size. If it travels through a narrowing microvessel stenosis successfully as in the healthy microvessel, the blood pressure must be increased. Clinical findings have indicated that retinal arteriolar narrowing is an important indicator for hypertension, [33], and is related to the risk of coronary heart disease, [34].

8 Conclusions

In the human blood circulatory system, macrovascular tissues represent only a small fraction of the system, while microvessels with diameters of the same size as RBCs number billion. In these capillaries, variations in mechanical properties of human RBCs lead to a number of human disease.

In the present study, dissipative particle dynamics method, as a mesoscopic numerical simulation technique combined with a coarse-grained spring network model of membrane, is employed to investigate the deformation and motion of a single RBC transiting through the microvessel stenosis. To confirm the feasibility of the method and the model, a RBC motion through the microfluidic channel was simulated and compared with the experiment. The deformation obtained in the simulation is consistent with the experimental results, which demonstrates the RBC

model has the basic capability to simulate behavior of large deformation in blood flow. Furthermore, the mechanical behavior of a single RBC in a rigid tube with stenosis was simulated. The results demonstrate that the RBC flows slowly when it enters the converging zone and it takes a long time for RBC to change in shape. However, less time is used for RBC exiting from the expanding zone. The RBC exhibits parachute-like shape in the straight tube and deforms into slipper shape or even bullet in order to fit in the narrowest zone. The relationship between RBC deformability and relative parameters such as the bending rigidity of cell membrane, driven force and the size of the stenosis was also investigated. When the bending rigidity of the membrane is raised, the fluidity of the RBC decreases. The RBC exhibits a large deformation if acted upon by the greater driven force, and has the longer transit time when the tube stenosis size is smaller.

For future studies, the model could be improved to account for the viscoelastic effects of the vessel walls. DPD method could be employed to implement the interactions between the flow and the deformable vessel walls. Moreover, the flow field and pressure field are required to investigate in detail. Currently, we intend to extend our simulations from a single RBC deformation to multiple RBCs aggregation deformation.

Acknowledgement: This work was supported by the National Natural Science Foundation of China (Grant No. 51276130, 10872152) and by the Specialized Research Fund for the Doctoral Program of Higher Education of China (Grant No. 20120072110037). The grants are gratefully acknowledged.

References

1. Li, J., Lykotrafitis, G., Dao, M. & Suresh, S. (2007) Cytoskeletal dynamics of human erythrocyte. *Proceedings of the National Academy of Sciences*, 104(12), 4937-4942.
2. Shelby, J. P., White, J., Ganesan, K., Rathod, P. K. & Chiu, D. T. (2003) A microfluidic model for single-cell capillary obstruction by *Plasmodium falciparum*-infected erythrocytes. *Proceedings of the National Academy of Sciences*, 100(25), 14618-14622.
3. Higgins, J. M., Eddington, D. T., Bhatia, S. N. & Mahadevan, L. (2007) Sick cell vasoocclusion and rescue in a microfluidic device. *Proceedings of the National Academy of Sciences*, 104(51), 20496-20500.
4. Hou, H. W., Bhagat, A. A. S., Chong, A. G. L., Mao, P., Tan, K. S. W., Han, J. & Lim, C. T. (2010) Deformability based cell margination-a simple

- microfluidic design for malaria-infected erythrocyte separation. *Lab on a Chip*, 10(19), 2605-2613.
5. Miller, L. H., Baruch, D. I., Marsh, K. & Doumbo, O. K. (2002): The pathogenic basis of malaria. *Nature*, 415(6872), 673-679.
 6. Drost, E. M., Kassabian, G., Meiselman, H. J., Gelmont, D. & Fisher, T. C. (1999) Increased rigidity and priming of polymorphonuclear leukocytes in sepsis. *American journal of respiratory and critical care medicine*, 159(6), 1696-1702.
 7. Pozrikidis, C. (2001) Effect of membrane bending stiffness on the deformation of capsules in simple shear flow. *Journal of Fluid Mechanics*, 440, 269-291.
 8. Pivkin, I. V. & Karniadakis, G. E. (2008) Accurate coarse-grained modeling of red blood cells. *Physical review letters*, 101(11), 118105-1-118105-4.
 9. Fedosov, D. A., Caswell, B. & Karniadakis, G. E. (2010) A multiscale red blood cell model with accurate mechanics, rheology, and dynamics. *Biophysical journal*, 98(10), 2215-2225.
 10. Pozrikidis, C. (1995) Finite deformation of liquid capsules enclosed by elastic membranes in simple shear flow. *Journal of Fluid Mechanics*, 297, 123-152.
 11. Shen, Z. Y. & He, Y. (2012) A Lattice Boltzmann Method for Simulating the Separation of Red Blood Cells at Microvascular Bifurcations. *Chinese Physics Letters*, 29(2), 024703-1-024703-4.
 12. Shi, X., Lin, G., Zou, J. & Fedosov, D. A. (2013) A lattice Boltzmann fictitious domain method for modeling red blood cell deformation and multiple-cell hydrodynamic interactions in flow. *International Journal for Numerical Methods in Fluids*, 72 (8), 895-911.
 13. Zhang, Z. G. & Zhang, X. W. (2011) Mechanical behavior of the erythrocyte in microvessel stenosis. *Science China Life Sciences*, 54(5), 450-458.
 14. Fedosov, D. A., Caswell, B. & Karniadakis, G. E. (2011) Wall shear stress-based model for adhesive dynamics of red blood cells in malaria. *Biophysical journal*, 100(9), 2084-2093.
 15. Noguchi, H.; Gompper, G. (2005) Shape transitions of fluid vesicles and red blood cells in capillary flows. *Proceedings of the National academy of Sciences of the United States of America*, 102(40), 14159-14164.

16. Vahidkhah, K. & Fatourae, N. (2012) Numerical simulation of red blood cell behavior in a stenosed arteriole using the immersed boundary–lattice Boltzmann method. *International Journal for Numerical Methods in Biomedical Engineering*, 28(2), 239-256.
17. Wang, T. & Xing, Z. W. (2013) Erythrocyte hemodynamics in stenotic microvessels: A numerical investigation. *Physical Review E*, 88(4), 042711-1-042711-9.
18. Suresh, S. (2007) Biomechanics and biophysics of cancer cells. *Acta Materialia*, 55(12), 3989-4014.
19. Yap, B. & Kamm, R. D. (2005) Mechanical deformation of neutrophils into narrow channels induces pseudopod projection and changes in biomechanical properties. *Journal of Applied Physiology*, 98(5), 1930-1939.
20. Guck, J., Schinkinger, S., Lincoln, B., Wottawah, F., Ebert, S., Romeyke, M. & Bilby, C. (2005) Optical deformability as an inherent cell marker for testing malignant transformation and metastatic competence. *Biophysical journal*, 88(5), 3689-3698.
21. Lee, G. Y. H. & Lim, C. T. (2007) Biomechanics approaches to studying human diseases. *Trends in biotechnology*, 25(3), 111-118.
22. Fischer, T. M. (2004) Shape memory of human red blood cells. *Biophysical journal*, 86(5), 3304-3313.
23. Abkarian, M., Faivre, M. & Viallat, A. (2007) Swinging of red blood cells under shear flow. *Physical review letters*, 98(18), 188302-1-188302-4.
24. Skotheim, J. M. & Secomb, T. W. (2007) Red blood cells and other non-spherical capsules in shear flow: oscillatory dynamics and the tank-treading-to-tumbling transition. *Physical review letters*, 98(7), 078301-1-078301-4.
25. Hoogerbrugge, P. J. & Koelman, J. (1992) Simulating microscopic hydrodynamic phenomena with dissipative particle dynamics. *EPL (Europhysics Letters)*, 19(3), 155-160.
26. Español, P. (1995) Hydrodynamics from dissipative particle dynamics. *Physical Review E*, 52, 1734-1742.
27. Groot, R. D. & Warren, P. B. (1997) Dissipative particle dynamics: Bridging the gap between atomistic and mesoscopic simulation. *The Journal of chemical physics*, 107(11), 4423-4435.

28. Fan, X., Phan-Thien, N., Chen, S., Wu, X. & Ng, T. Y. (2006) Simulating flow of DNA suspension using dissipative particle dynamics. *Physics of Fluids*, 18(6), 063102-01-063102-10.
29. Allen, M. P. & Dominic, D. J. (1989) *Computer simulation of liquids*. Oxford university press.
30. Pozrikidis, C. (2010) *Computational hydrodynamics of capsules and biological cells*. CRC Press.
31. Mai-Duy, N., Pan, D., Phan-Thien, N. & Khoo, B. C. (2013) Dissipative particle dynamics modeling of low Reynolds number incompressible flows. *Journal of Rheology*, 57(2), 585-603.
32. Kaoui, B., Biro, G., Misbah, C. (2009) Why do red blood cells have asymmetric shapes even in a symmetric flow? *Physical review letters*, 103(18), 188101-1-188101-4.
33. Smith, W., Wang, J. J., Wong, T. Y., Rohtchina, E., Klein, R., Leeder, S. R. & Mitchell, P. (2004) Retinal arteriolar narrowing is associated with 5-year incident severe hypertension the Blue Mountains Eye Study. *Hypertension*, 44(4), 442-447.
34. Wong, T. Y., Klein, R., Sharrett, A. R., Duncan, B. B., Couper, D. J., Tielsch, J. M. & Hubbard, L. D. (2002) Retinal arteriolar narrowing and risk of coronary heart disease in men and women. *JAMA: the journal of the American Medical Association*, 287(9), 1153-1159.

